

Characterizing Frictional Contact Loading via Isochromatics

K.V.N. Surendra · K.R.Y. Simha

Received: 29 August 2013 / Accepted: 11 February 2014 / Published online: 25 March 2014
© Society for Experimental Mechanics 2014

Abstract Isochromatic patterns in the vicinity of frictional contacts furnish vital clues for characterizing friction. Though friction effects are evident in a diametrically loaded circular disk, three-point loading provides better results towards highlighting friction. In this paper, a new method of characterizing friction at loading contacts using photoelastic isochromatics patterns is presented. Location of isotropic points (IPs) formed in three-point and four-point loadings of circular disk is used as a main tool to quantify the friction component using theoretical analysis. Bifurcation of isochromatic fringe loops near the distributed loads is explained by the presence of anti-symmetric Hertzian shear traction in addition to Hertzian normal traction. The classical solution by Flamant for point load at the edge of half plane is used to derive stresses in circular disk for all required loading configurations. A semicircular ring under three-point loading is examined using photoelasticity to understand the isochromatics pattern theoretically by considering normal and shear traction components at loaded regions.

Keywords Isochromatics · Friction · Hertzian load · Isotropic point (IP) · Flamant solution

Electronic supplementary material The online version of this article (doi:10.1007/s11340-014-9865-3) contains supplementary material, which is available to authorized users.

K.V.N. Surendra (✉) · K.R.Y. Simha
Photoelasticity Laboratory, Department of Mechanical Engineering, Indian Institute of Science, Bangalore 560012, India
e-mail: kvns@mecheng.iisc.ernet.in

K.R.Y. Simha
e-mail: simha@mecheng.iisc.ernet.in

Introduction

Frictional contact loading accompanied by both normal and shear stresses in general remains unknown for all finite contacts. Only in some fortunate cases can one experimentally access the existing state of stress. Pioneering work by Dally and Chen [1] established the photoelastic technique to measure frictional contact forces at asperities. They were able to recover the individual loads at the asperities from the far-field fringes. There is a need to characterize the stress field in the immediate vicinity of asperities to supplement contact mechanics research. This paper makes an attempt to exploit the distortions caused by friction on isochromatic patterns in general and isotropic points (IPs) in particular. Hertzian contact conditions with friction are modeled theoretically for interpreting experimental isochromatics.

Earlier, few researchers used photoelasticity for studying friction related problems. For example, Uemura et al. [2, 3] determined coefficients of static and kinetic friction by measuring normal and shear traction components at contact using photoelastic method and compared the coefficients against those obtained by direct method. But they did not describe the method to obtain the traction components using photoelasticity. As another example, Maria [4] explored the nature of singularity that arises during frictional slip of a wedge on a half-plane using Mellin transform and validated the analysis using isochromatic results. Burguete and Patterson [5] studied a cylinder in contact with half-space using stress freezing. They demonstrated the control of inter-facial friction achieved by the photoelastic stress freezing. Fedorchenko et al. [6] employed photoelastic technique to investigate contact stresses in powder compaction. They obtained normal and frictional shear stress distributions on the die walls from photoelastic results. Similarly, Barbat and Rao [7] investigated the contact stresses at



interface between synthetic sapphire die and work piece of a strip drawing operation by studying isochromatics and isoclinics patterns of the transparent die. Foust et al. [8] used photoelasticity to measure boundary tractions at a bolted joint from which individual stress components were determined considering friction at the interface by formulating the problem in the form of a series of Airy stress function. Recent work by Guan et al. [9] suggested substitutes for photoelastic method to study relation between friction coefficient and asperities inclination.

Conventional photoelastic understanding of a diametrically loaded circular disk is limited to the central region away from the loads. Point loads are assumed and the effect of frictional contact loading is not important in conventional analysis. As a historical prelude, the frontispiece in the first volume of the 1941 classic text by Frocht [10] analyzed in detail on page 191, assumes frictionless supports to study the IPs. However, there is a need for including Hertzian loading zones including friction to better interpret the isochromatic patterns near the loading zones. The importance of friction during loading and unloading are clearly evident in many engineering applications such as fretting [11] often leading to catastrophic crack propagation. It is therefore interesting to predict the characteristics of isochromatics analytically to interpret experimental patterns. Here, we revisit the problem considered by Frocht [10] experimentally in order to recapture and reinterpret the effect of friction on IPs.

Regarding the method of solution for stresses in *plane* problems, generalized solution was established four decades ago [12, 13]. The generalized solution was evolved from many elasticians out of which Flamant solution gave ways to solve many contact mechanics problems [14]. The classic text by Coker and Filon [15] provides various ways of solving elasticity problems using photoelasticity in conjunction with theoretical analysis. A few classical solutions for circular disk problems are recalled here. Michell [16] solved the problem of circular disk under two collinear point loads one acting at center and the other at periphery. Mindlin [17] extended Michell's solution to the disk with the inner load acting at any radial position using inversion transformation. Such simple solutions are seldom possible for non-circular and annulus problems for which cases infinite series' are helpful. In this regard, Ma and Hung [18] solved circular disk under uniform pressure on part of its boundary using series solution. Surendra and Simha [19] solved semi-circular disk loaded *symmetrically* at its curved boundary using a truncated series. Modeling real loads as Hertzians is usual. As an example, Dini and Hills [20] analyzed frictional dissipation during rough axisymmetric Hertzian contact of a sphere with half-space by considering an oscillatory shear whose magnitude is always less than that causes sliding.

Photoelastic technique was recently employed to explore similar parameters in stress analysis. For instance, Ayatollahi et al. [21] and Mirsayar et al. [22] used photoelasticity for analyzing singularity of stresses near bi-material sharp notches. Further, Mirsayar [23] calculated stress intensity factors for the inter-facial notch in a bi-material joint of a Brazilian disk with square notch. Zakeri et al. [24], using photoelasticity, studied T-stress in cracked Brazilian disk loaded under mode-II.

The main aim of the present investigation is to introduce a new method for quantifying friction at loading contacts using information of IPs alone in the isochromatic fringe field. This is achieved through the use of analytical solution of circular disk under in-plane loading in conjunction with photoelastic results of the disk under two different loading configurations. The present work also aims to explain splitting of fringes at close vicinity of distributed loading contacts in an isochromatic field. Distortion caused by the friction in case of a semicircular ring under a loading is also studied. All the experiments are conducted at room temperature. Analytical solutions for circular disk and semicircular ring are derived within the scope of linear elasticity without considering body forces.

Photoelastic Experiments

Photoelastic experiments conducted towards studying the effect of friction on isochromatics patterns are explained in this section. Conventional arrangement of circular polariscope with quarter-wave plates on either sides of loaded test specimen as shown in Fig. 1 is used to obtain isochromatic patterns. A monochromatic light source which uses sodium vapor is used as the first element of a polariscope as shown in the figure. The orientations of polarizer and analyzer of

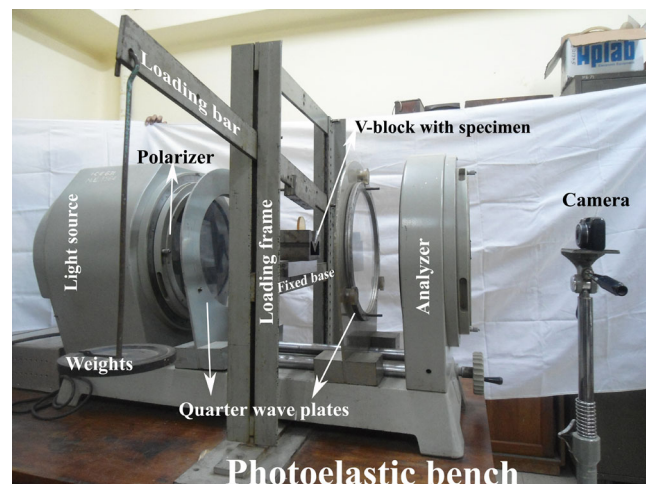


Fig. 1 Circular polariscope arrangement

the polariscope are kept perpendicular to each other to get dark-field fringes.

Specimen in all experiments is loaded using a lever-arm mechanism mounted on the loading frame as shown in Fig. 1 to magnify the applied loads. Specimen is loaded at the top by a steel bar which is hinged at one of its ends and weights are placed at its other end. The self weight of the top steel bar is balanced by a dead load placed near the hinged end. Lever-arm ratio of the mechanism, is calculated to be 3.55 by measuring various distances along the loading bar.

Specimens Fabrication

The specimens were fabricated by cold casting. Two Perspex plates each of thickness 0.5 inch were used to prepare the mold. Since the required thickness of all specimens used

in this paper was 6 mm, the two Perspex plates were fixed to each other with a parallel separation of 6 mm. The plates were clamped parallel at three of its sides. The fourth side was kept open for pouring molten resin. The inner surfaces of Perspex plates were smeared by silicon grease, a mold releasing agent which also helped in obtaining a scratch-free surfaces of specimens.

Epoxy resin ($C_{21}H_{25}ClO_5$, polymer that contain an oxirane group) and Triethylene Tetramine that hardens the resin were taken in the ratio of 100 : 9 by weight. The commercial name of the epoxy resin used is *Lapox C-51* and that of the hardener is *Lapox K-6* both of which are purchased from local manufacturer *Atul Ltd.* The hardener was added to the resin slowly; and the mix was stirred with a glass rod taking care to avoid air bubbles. The mixture was poured into the mold kept vertically along its wall. The complete setup was undisturbed for two days. Then the polymerized sheet was taken out of the mold and following shapes and sizes of test specimens were cut from the sheet by machining: A semicircular ring of outer diameter 241 mm and inner diameter 100.5 mm and a circular disk of diameter 60 mm for calibrating the material for material fringe constant f_σ as well as for new experiments, as shown in Fig. 2. Residual stresses were induced during machining which were removed by the process of annealing. In the process, the specimens were heated in an oven to softening temperature of the material which is around 140 °C and soaked at this temperature for 5 hours. The specimens were then cooled to the room temperature at a rate of -3 °C/hour inside the oven.

The set of specimens shown in Fig. 2(a) are used for three-point loading configuration. We designate the specimens by Type-A. And the specimen shown in Fig. 2(b) is designated by Type-B which is used for four-point loading as explained in section “[Isochromatic Results](#)”.

Calibration of the Specimens for f_σ

Isochromatics are contours of $(\sigma_1 - \sigma_2)$, difference of *in-plane* principal stresses. According to second law of photoelasticity, photoelastic fringe order N is related to $(\sigma_1 - \sigma_2)$ as follows.

$$\sigma_1 - \sigma_2 = \frac{Nf_\sigma}{h} \quad (1)$$

where f_σ is photoelastic material fringe constant which is subjected to change over the time due to aging of the material.

The two specimens mentioned previously were calibrated at the time of experimenting for isochromatics. The theoretical solution of circular disk under two diametral point loads was used for calibration which is a usual practice [25]. The

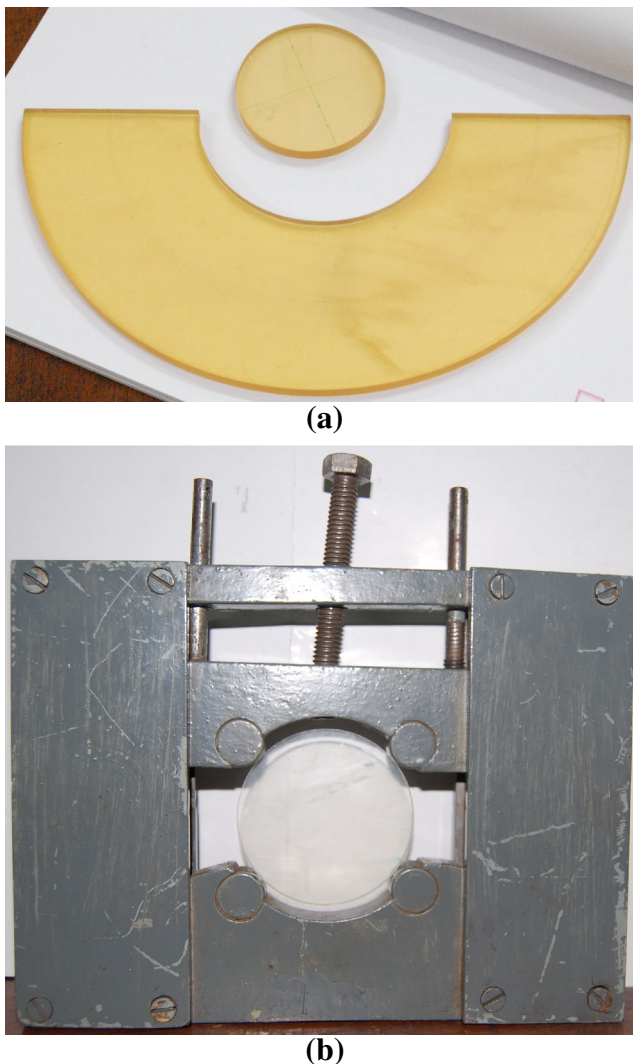


Fig. 2 Fabricated specimens (a) Type-A: Circular disk of 60 mm diameter and Semicircular ring of 100.5 mm ID and 241 mm OD (b) Type-B: Circular disk in the fixture for four-point loading

difference of principal stresses at the center of the disk is given by:

$$\sigma_1 - \sigma_2 = \frac{4P}{\pi Rh} \quad (2)$$

where P is total applied load, R is radius of the disk and h is thickness of the disk. From equations (2) and (1) and noting that radii of the disks is $R = 0.03$ m, f_σ can be written as:

$$f_\sigma = \frac{4P}{\pi RN} = 42.44 \left(\frac{P}{N} \right) \text{ N/m/fringe} \quad (3)$$

Various loads are applied incrementally and for each load, fringe order at center of the disk is read manually using method of compensation [25]. Compensation method is used for finding the real value of fringe order when a non-integer fringe order forms at a point of interest. We are well aware that dark fringes in the dark-field set up corresponds to integer fringe orders ($N = 0, 1, 2, \dots$) for which optical axes of polarizer and analyzer must be 90° apart. When the axes are aligned (0°), the dark fringes correspond to half fringe orders ($N = 0.5, 1.5, 2.5, \dots$). When the axes of polarizer and analyzer are separated by, in general, θ , the fractional fringe order of the dark fringes can be written as $N_{\text{frac}} = 0.5 - 0.5 \times \theta/90^\circ$. Thus, when no dark fringe passes through the point of interest, we can rotate the analyzer with respect to polarizer to an extent that a dark fringe passes through the point. If we note the angle of rotation and which fringe order in dark-field set up moves to the point upon rotation, we can determine the required non-integer fringe order by adding or subtracting the fraction to the original integer value. Adding or subtracting depends on whether the rotation is clock-wise or counter clock-wise. This is how we compensate for N_{frac} in the method.

Fringe orders are read at the center of the disk while loading (N_{load}) as well as unloading (N_{unload}) for all applied

loads (P). Average fringe orders (N_{avg}) are calculated as $(N_{\text{load}} + N_{\text{unload}})/2$ for all P and plotted along x -axis as shown in Fig. 3. A straight line passing through origin is fitted to the experimental data of each specimen using method of least-squares and superimposed in each of the plots. MATLAB is used for curve fitting. The slope of the straight-line fit is obtained to be 325.6 and 253.8 for Type-A and Type-B specimens respectively. The slope values are substituted for P/N in equation (3) to get required fringe constants $f_\sigma^A = 13819$ N/m/fringe and $f_\sigma^B = 10772$ N/m/fringe. f_σ^A will be used for plotting isochromatic patterns from theoretical solutions in sections “Three-Point Loading Results” and “Elasticity Solution of Semicircular Ring”, and f_σ^B will be used in section “Four-Point Loading Results”.

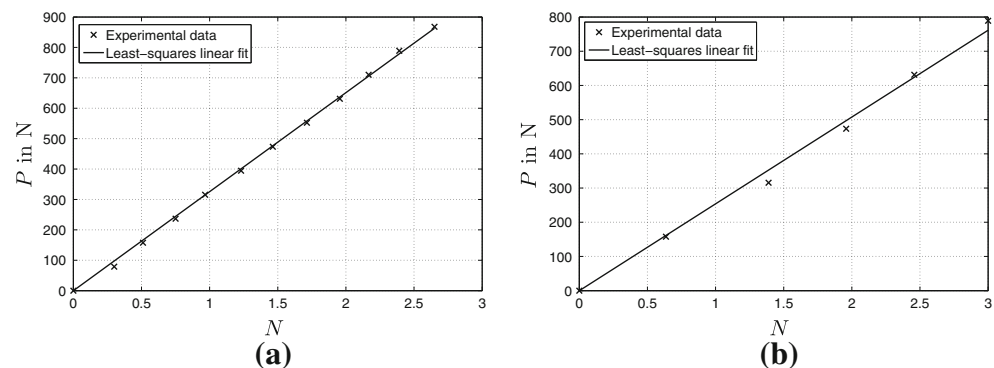
Isochromatic Results

Isochromatics are recorded for three different experiments which are as follows: Circular disk under three-point loading, the disk under four-point loading and semicircular ring under three-point loading. Three-point loading of the disk is done by using a V-block as shown in Fig. 4. The included angle of V-block is 90° . The V-block is made of hardened Cast Iron.

For a load of $P = 790$ N, isochromatics are shown in Fig. 5. Note that the line markings appearing on the specimen along its two perpendicular diameters are not aligned with the symmetry of the loading. It can be observed from the figure that *zeroth order fringe* (ZOF) forms along periphery at top portion and it moves inwards at bottom portion.

Isotropic point (IP) is an isolated point in isochromatic fringe field where $\sigma_1 = \sigma_2$ or ZOF ($N = 0$) is formed. Fringe order (N) increases in any direction around, from zero at IP. As a special case of ZOF, IP is in contrast to the general nature of ZOF which may form along a curve.

Fig. 3 Calibration curves for f_σ of specimens materials, P versus N_{avg} : (a) Type-A (b) Type-B



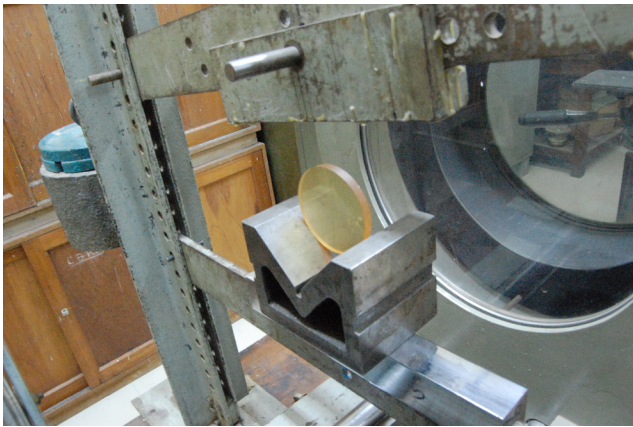


Fig. 4 Three-point loading of circular disk using V-block in polariscope

There is an IP on the axis of symmetry below the center, partially enveloped by first order fringe ($N = 1$) in Fig. 5. Distance of IP from the center, y_{iso}^{exp} is measured manually using a ruler by magnifying the image of isochromatics pattern. Magnification is calibrated by mapping the disk diameter to its actual value of 60 mm. The distance y_{iso}^{exp} relative to disk radius is calculated to be:

$$\frac{y_{iso}^{exp}}{R} = \frac{9.54}{30} = 0.318 \tag{4}$$

which will be used in section “[Three-Point Loading Results](#)” for identifying friction coefficient at the supports of the disk.

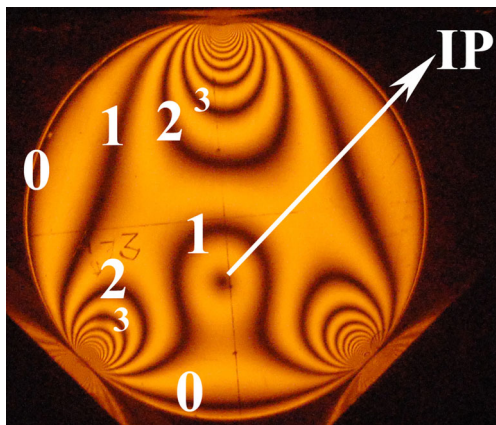


Fig. 5 Experimental isochromatics of circular disk under three-point loading symmetric about vertical diameter

As the second experiment, circular disk under four-point loading is considered. The disk is loaded using a fixture shown in Fig. 2(b). The fixture is loaded from the top of the fixture’s slider in a lever-arm mechanism using a top steel bar as shown in Fig. 2(b). The fixture is made of mild steel and its surface is painted. The top load on the fixture’s slider is balanced by two reactions by the disk specimen at the bottom portion of fixture’s slider. This is schematically shown in Fig. 6.

Here, inclination of the reactions on to the slider are not known *a priori* like in case of three-point loading. This is why a general loading situation of *non-zero* friction is shown in the figure. Isochromatics pattern of the disk under four-point loading for a top load of $P = 869$ N is shown in Fig. 7. There are two IPs formed along the horizontal diameter symmetrically on either side of the vertical diameter of the disk. First order fringe completely envelops the pair of IPs. Similar to three-point loading case, here also ZOF moves inwards from top and bottom portions between load points.

Ideally, the four-point loading shown in Fig. 2(b) and consequently the isochromatics pattern in Fig. 7 are supposed to exhibit four-fold symmetry (symmetric about horizontal and vertical diameters of the disk or x and y axes). Due to inevitable experimental inaccuracies, these symmetries are slightly disturbed. However, the positions of the load points on the disk periphery could be determined by manually measuring the inter-point distances using a ruler, in the image of isochromatic patterns (Fig. 2(b)). The image is magnified enough for improving measurement accuracy and the magnification is calibrated by mapping disk diameter in the image to actual value of 60 mm. Various distances

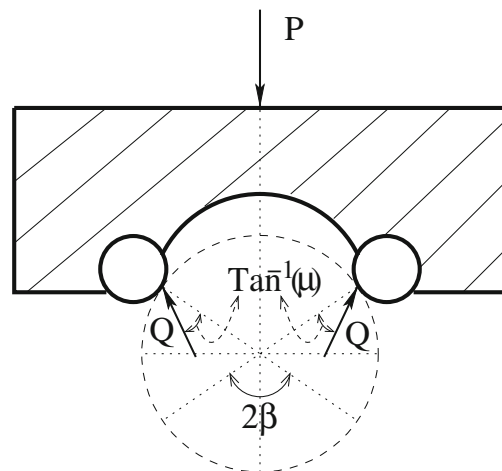


Fig. 6 Free-body diagram of fixture’s slider

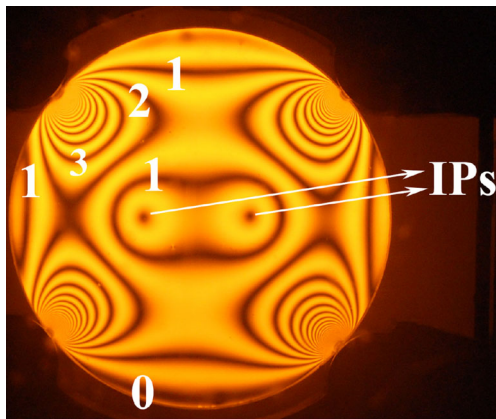


Fig. 7 Experimental isochromatics of circular disk under four-point loading $P = 869$ N

in the magnified image including disk diameter is given below, the symbols being referred to Fig. 8.

$$\begin{aligned} 2R &= 16.4 \text{ cm}, & 2a &= 4.45 \text{ cm}, & \overline{AB} &= 12.4 \text{ cm} \\ \overline{BC} &= 11.2 \text{ cm}, & \overline{CD} &= 12.2 \text{ cm}, & \overline{DA} &= 10.6 \text{ cm} \end{aligned} \quad (5)$$

The magnitude and direction of the forces transmitted from fixture's slider to the specimen will be determined in section “Four-Point Loading Results” using theoretical interpretation of isochromatics pattern of Fig. 7. Each of the two bottom reactions on the disk from the fixed pins of fixture (Fig. 2(b)) are equal to the top ones due to the symmetry about the x -axis.

As the third experiment, semicircular ring under three-point loading is considered. Again, V-block is used for bottom supports. Distance between the top edges of the V-block is measured to be 72 mm. With this and knowing the V-block angle to be 90° and outer diameter of the ring to be 241 mm, the included angle of support points on the ring's

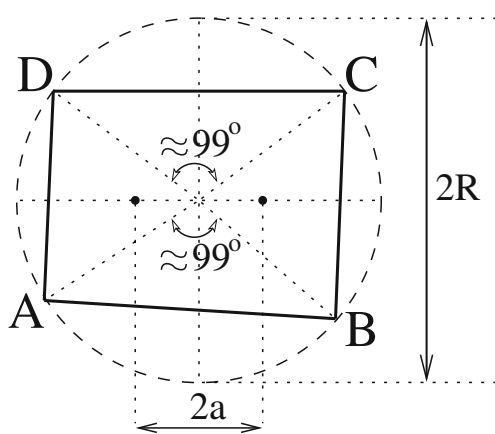


Fig. 8 Cyclic quadrilateral formed by the four points of loading on the disk periphery

outer boundary at its center is found to be $2\beta^{ring} = 34.8^\circ$. This included angle will be used in section “Results of Analysis” for deriving analytical solution for the ring problem. To facilitate loading at the top, a calibration disk is placed on the inner boundary of the ring which transmits the load from top steel bar to the inner boundary. Load is assumed to transmit between calibration disk and the ring in Hertzian way through finite area of contact since the surfaces are conforming type (concave-convex) but of different curvatures. A Hertzian load essentially has an elliptical variation of load along contact length. It is defined for the ring problem in mathematical terms in section “Results of Analysis” as equation (33). For a top load of $P = 790$ N, isochromatics pattern is shown in Fig. 9(a). The three-point loading of the ring is shown schematically in Fig. 9(b) with point loads in place of Hertzian loads.

Isochromatics pattern in the calibration disk from Fig. 9(a) is as expected. Fringe pattern at close vicinity of supports from the V-block edges, may not be so clear to identify all the fringe orders formed, due to lack of required resolution. However, fringe patterns in the calibration disk and the ring at their contact are clearly identifiable and it can be observed that maximum fringe order near the disk-ring contact is $N = 7$ in both specimens. ZOF occupies most of the region of the ring. No IPs can be observed in the ring. First order fringe formed in the ring resembles the shape of English alphabet ‘A’.

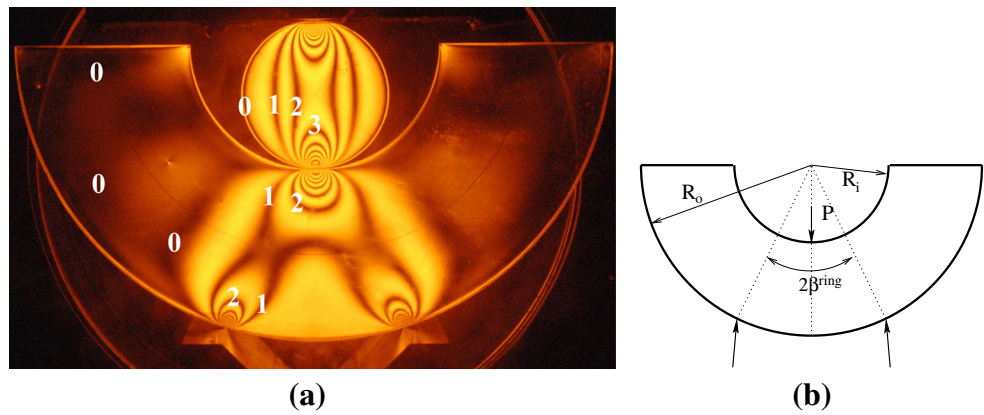
Elasticity Solution of Circular Disk under Periphery Loading

Closed form elasticity solution of circular disk loaded at its boundary is derived in this section. Firstly, expressions for stresses in semi-infinite plate with point load with respect to a general coordinate system, are derived. These general expressions are then used to derive stresses in circular disk under periphery loading making use of superposition principle. Isochromatics are plotted for various loading cases of point loads as well as Hertzian loads with focus on three-point and four-point symmetric loadings.

Method

Surendra [26] proved that the solution for a circular disk under any self-equilibrating in-plane oblique loads on its periphery can be derived by superposing Flamant solutions along with a hydrostatic solution. The same method is used here which uses superposition principle, to derive stress components for all the loading cases of circular disk by using Flamant solution as the base. It will be evident that the method is simple yet giving closed form solutions. It is well known that a circular disk under two diametral

Fig. 9 (a) Isochromatics of semicircular ring under three-point loading using a calibration disk and V-block (b) Schematic of ring for load angle



point loads at periphery was derived by Hertz [12] as follows.

A semi-infinite plane is assumed at each of the point loads in such a way that its straight boundary is tangential to the circular boundary of the disk, with the point load coinciding with that on the semi-infinite plane. The two states of stress due to the two point loads are superposed. The resulting non-zero traction on the boundary of the disk is annihilated using the hydrostatic solution. A similar procedure is adopted here to obtain the solution of circular disk under any periphery loading. Airy stress function is defined for 2D elasticity problems without considering body forces in terms of polar coordinates as follows [12].

$$\begin{aligned} \sigma_{rr} &= \frac{1}{r^2} \frac{\partial^2 \phi}{\partial \theta^2} + \frac{1}{r} \frac{\partial \phi}{\partial r} \\ \sigma_{\theta\theta} &= \frac{\partial^2 \phi}{\partial r^2} \\ \tau_{r\theta} &= -\frac{\partial}{\partial r} \left(\frac{1}{r} \frac{\partial \phi}{\partial \theta} \right) \end{aligned} \tag{6}$$

Flamant problem is a semi-infinite plane with a point load on its straight boundary. The solution to the problem with an inclined point load, is given [12] with respect to the coordinate system shown in Fig. 10(a) in terms of Airy stress function by:

$$\phi^{(a)}(r_1, \theta_1) = \frac{-P}{\pi h} r_1 (\gamma + \theta_1) \sin(\gamma + \theta_1) \tag{7}$$

where h is the thickness of the disk and the superscript (a) indicates that the solution corresponds to sub-figure (a).

Solution for the problem with respect to a different coordinate system, for convenience while superposing, can be obtained by sequence of rotations and translations of coordinates. Since Airy stress function is a scalar function, it is invariant with a change of coordinate system. If we were to transform, instead of Airy function, the stress components describing the solution, we had to transform the stress tensor using appropriate equations [12]. In any case, coordinates in which solution is described, need to be updated, whenever a change occurs.

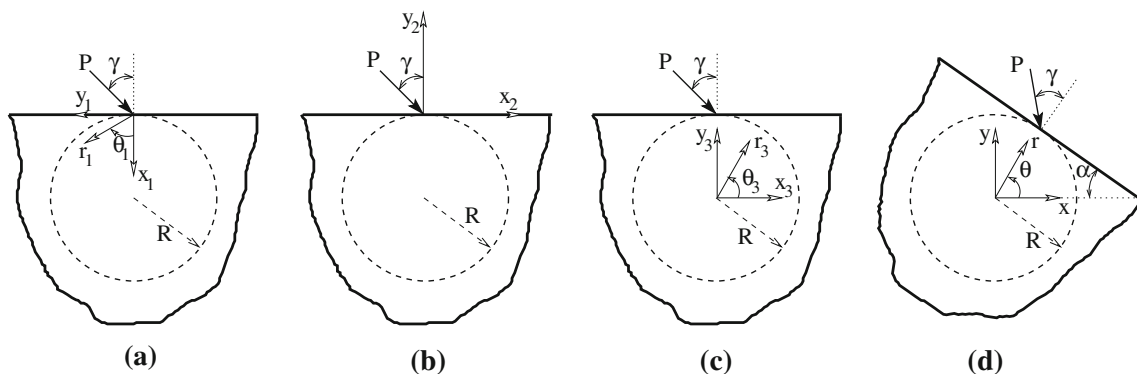


Fig. 10 Normal point load at the boundary of a half plane (Flamant problem) shown with different coordinate systems and hypothetical circular disk boundary

The solution presented in equation (7) is gradually transformed to required coordinates as explained in set of equations (8). In brackets of each equation in equations

set (8), change of coordinates affected from previous coordinate system is mentioned.

$$\begin{aligned}
 \phi^{(a)}(x_1, y_1) &= \frac{-P}{\pi h} \left(\gamma + \arctan \frac{y_1}{x_1} \right) (x_1 \sin \gamma + y_1 \cos \gamma) & \left(\because r_1 \rightarrow \sqrt{x_1^2 + y_1^2}, \theta_1 \rightarrow \arctan \frac{y_1}{x_1} \right) \\
 \phi^{(b)}(x_2, y_2) &= \frac{P}{\pi h} \left(\gamma + \arctan \frac{x_2}{y_2} \right) (y_2 \sin \gamma + x_2 \cos \gamma) & (\because x_1 \rightarrow -y_2, y_1 \rightarrow -x_2) \\
 \phi^{(c)}(x_3, y_3) &= \frac{P}{\pi h} \left(\gamma + \arctan \left(\frac{x_3}{y_3 - R} \right) \right) ((y_3 - R) \sin \gamma + x_3 \cos \gamma) & (\because x_2 \rightarrow x_3, y_2 \rightarrow y_3 - R) \\
 \phi^{(c)}(r_3, \theta_3) &= \frac{P}{\pi h} \left(\gamma + \arctan \left(\frac{r_3 \cos \theta_3}{r_3 \sin \theta_3 - R} \right) \right) ((r_3 \sin \theta_3 - R) \sin \gamma + r_3 \cos \theta_3 \cos \gamma) & (\because x_3 \rightarrow r_3 \cos \theta_3, y_3 \rightarrow r_3 \sin \theta_3) \\
 \phi^{(d)}(r, \theta) &= \frac{P}{\pi h} \left(\gamma + \arctan \left(\frac{r \cos(\alpha + \theta)}{r \sin(\alpha + \theta) - R} \right) \right) ((r \sin(\alpha + \theta) - R) \sin \gamma + r \cos(\alpha + \theta) \cos \gamma) & (\because r_3 \rightarrow r, \theta_3 \rightarrow \alpha + \theta)
 \end{aligned} \tag{8}$$

Using equation (6), stresses corresponding to $\phi^{(d)}(r, \theta)$ are derived which read after simplification:

$$\begin{aligned}
 [\tilde{\sigma}^{(d)}](r, \theta) &= \begin{bmatrix} \sigma_{rr}^{(d)} & \tau_{r\theta}^{(d)} \\ \tau_{r\theta}^{(d)} & \sigma_{\theta\theta}^{(d)} \end{bmatrix} = -2P \times \frac{R \cos \gamma - r \sin(\alpha - \gamma + \theta)}{\pi h \{r^2 + R^2 - 2rR \sin(\alpha + \theta)\}^2} \\
 &\times \begin{bmatrix} (r - R \sin(\alpha + \theta))^2 & -R \cos(\alpha + \theta)(r - R \sin(\alpha + \theta)) \\ -R \cos(\alpha + \theta)(r - R \sin(\alpha + \theta)) & R^2 \cos^2(\alpha + \theta) \end{bmatrix} \tag{9}
 \end{aligned}$$

Flamant solution (equation (9)) in this form, will be used to derive all further periphery loadings of circular disk. To demonstrate the efficacy of the method described, well-known solution of diametral compression of circular disk (Hertz solution, [12]) is derived using equation (9) as follows. Solution is written schematically as:

$$\begin{aligned}
 [\tilde{\sigma}^{\text{DiaComp}}] &= [\tilde{\sigma}^{(d)}]_{\substack{\alpha=0^\circ \\ \gamma=0^\circ}} + [\tilde{\sigma}^{(d)}]_{\substack{\alpha=180^\circ \\ \gamma=0^\circ}} + \frac{P+P}{2\pi Rh} \begin{bmatrix} 1 & 0 \\ 0 & 1 \end{bmatrix} \\
 &\tag{10}
 \end{aligned}$$

where the subscripts, given outside a tensor [·], indicates substitution for the parameters. The same convention is used throughout the paper for substitution. The last term in equation (10) is to annihilate the hydrostatic compressive stress induced on the boundary due to first two (Flamant) terms. $\gamma = 0^\circ$ for both the loads as they are normal to the boundary. Since the two loads are acting diametrically opposite, $\alpha = 0^\circ$ for one load and $\alpha = 180^\circ$ for the other. After simplification, solution for diametral compression reads as in equation (11) which exactly coincides with the solution given in standard text [12].

$$\begin{aligned}
 \sigma_{rr}^{\text{DiaComp}} &= \frac{-2P}{\pi h} \left[\frac{(R - r \sin \theta)(r - R \sin \theta)^2}{\{r^2 + R^2 - 2rR \sin \theta\}^2} + \frac{(R + r \sin \theta)(r + R \sin \theta)^2}{\{r^2 + R^2 + 2rR \sin \theta\}^2} - \frac{1}{2R} \right] \\
 \sigma_{\theta\theta}^{\text{DiaComp}} &= \frac{-2P}{\pi h} \left[\frac{(R - r \sin \theta)R^2 \cos^2 \theta}{\{r^2 + R^2 - 2rR \sin \theta\}^2} + \frac{(R + r \sin \theta)R^2 \cos^2 \theta}{\{r^2 + R^2 + 2rR \sin \theta\}^2} - \frac{1}{2R} \right] \\
 \tau_{r\theta}^{\text{DiaComp}} &= \frac{-2PR \cos \theta}{\pi h} \left[\frac{(R - r \sin \theta)(-r + R \sin \theta)}{\{r^2 + R^2 - 2rR \sin \theta\}^2} + \frac{(R + r \sin \theta)(r + R \sin \theta)}{\{r^2 + R^2 + 2rR \sin \theta\}^2} \right] \tag{11}
 \end{aligned}$$

Three-Point Loading Results

Using Flamant solution (9), circular disk under three normal loads on its boundary symmetric to y -axis is solved using linear superposition principle as shown in Fig. 11. A semi-infinite plate is assumed at each of the point loads and the stresses are superposed after appropriate coordinate transformations. This is realized by choosing right values for rotation angle α and load angle γ in equation (9) (Fig. 10(d)) for each of the sub-problems and adding them up as follows.

$$[\tilde{\sigma}^{3N(1)}] = [\tilde{\sigma}^{(d)}]_{\substack{\alpha=0^\circ \\ \gamma=0^\circ \\ P=Q}} + [\tilde{\sigma}^{(d)}]_{\substack{\alpha=\beta \\ \gamma=0^\circ \\ P=Q}} + [\tilde{\sigma}^{(d)}]_{\substack{\alpha=-\beta \\ \gamma=0^\circ \\ P=Q}} \quad (12)$$

where $\gamma = 0^\circ$ for all the loads since they are acting normal to the boundary. For the disk to be in static equilibrium in this loading configuration (refer to Fig. 11(a)), $Q = -P/(2 \cos \beta)$. Superposed solution equations (12) would leave a constant radial stress of magnitude $(P + 2Q)/(2\pi Rh)$ on the circular boundary as follows.

$$[\tilde{\sigma}^{3N(1)}]_{(r=R)} = \begin{bmatrix} -\frac{P+2Q}{2\pi Rh} & 0 \\ 0 & 0 \end{bmatrix} \quad (13)$$

Observe that the residual stresses on the boundary after superposing the Flamant problems do not depend on θ . In general, any self equilibrating loading on the boundary of the disk would induce a constant radial stress at the boundary just after superposing the Flamant problems. Magnitude of the residual radial stress at the boundary would be $\sum P^{(N)}/(2\pi Rh)$ where $\sum P^{(N)}$ is sum of all normal components of the forces acting on the boundary.

Hydrostatic solution is used for annihilating the residual stresses on the boundary as it can serve the purpose in all cases of self-equilibrating boundary loading. Airy function for hydrostatic state of stress (given in equation (14)) is $\phi^{Hy} = c_0 r^2$ where c_0 is constant that can be so chosen

as to satisfy the boundary condition and is equal to $(P + 2Q)/(4\pi Rh)$ for our problem.

$$[\tilde{\sigma}^{Hy}] = \begin{bmatrix} \sigma_{rr}^{Hy} & \tau_{r\theta}^{Hy} \\ \tau_{r\theta}^{Hy} & \sigma_{\theta\theta}^{Hy} \end{bmatrix} = \begin{bmatrix} 2c_0 & 0 \\ 0 & 2c_0 \end{bmatrix} = \frac{P+2Q}{2\pi Rh} \begin{bmatrix} 1 & 0 \\ 0 & 1 \end{bmatrix} \quad (14)$$

Superposing hydrostatic solution (equation (14)) with equation (12) gives the required stresses, given below and shown in Fig. 11 schematically, in the circular disk under three-point normal loading symmetric about y -axis. Explicit equations for stresses are not shown here since they are unwieldy.

$$[\tilde{\sigma}^{3N}] = [\tilde{\sigma}^{3N(1)}] + [\tilde{\sigma}^{Hy}] \\ = [\tilde{\sigma}^{N(d)}]_{\substack{\alpha=0 \\ P=Q}} + [\tilde{\sigma}^{N(d)}]_{\substack{\alpha=\beta \\ P=Q}} \\ + [\tilde{\sigma}^{N(d)}]_{\substack{\alpha=-\beta \\ P=Q}} + [\tilde{\sigma}^{Hy}] \quad (15)$$

Isochromatics of the disk under three-point loading for $\beta = 120^\circ$ and $\beta = 135^\circ$ are shown in Fig. 12 which are obtained using equation (15) taking $f_\sigma = f_\sigma^A$ from last paragraph of section “Calibration of the Specimens for f_σ ”.

From Fig. 12, clearly IP moves along axis of symmetry from center of the disk when $\beta = 120^\circ$ towards periphery as β is increased. Note that $N = 0$ also forms along throughout boundary and there is only one IP in the disk under the loading. The position of IP, in terms of its y -coordinate, y_{iso} is obtained by solving the following equation numerically using MATHEMATICA software for various cases of β .

$$\sigma_{rr}^{3N}(\theta = \pi/2) = \sigma_{\theta\theta}^{3N}(\theta = \pi/2) \text{ when } 90^\circ \leq \beta \leq 120^\circ \\ (\because \tau_{r\theta}^{3N}(\theta = \pi/2) = \tau_{r\theta}^{3N}(\theta = -\pi/2) = 0) \\ \sigma_{rr}^{3N}(\theta = -\pi/2) = \sigma_{\theta\theta}^{3N}(\theta = -\pi/2) \text{ when } 120^\circ \leq \beta \leq 180^\circ \quad (16)$$

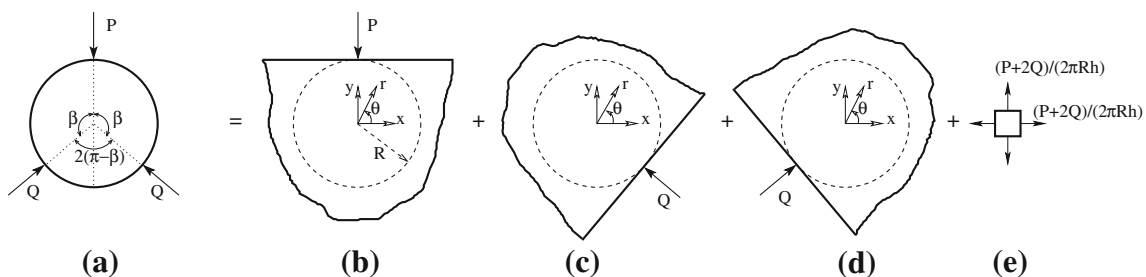


Fig. 11 Circular disk under three-point symmetric loading: Solution algorithm

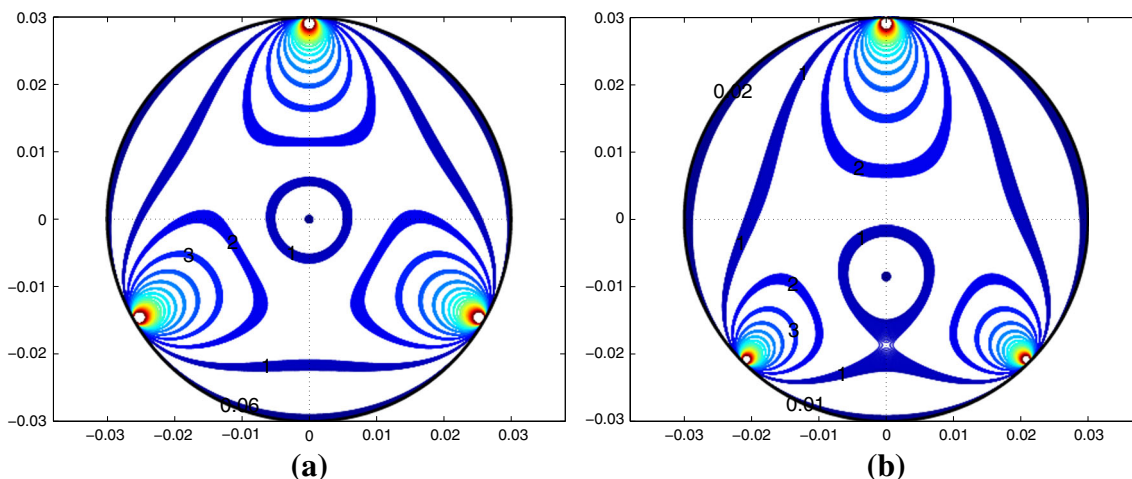


Fig. 12 Isochromatics of circular disk under 3 point normal loading for (a) $\beta = 120^\circ$ (b) $\beta = 135^\circ$

y_{iso} is plotted against β in Fig. 13 to see the effect of β when only normal loads are acting on the disk.

If we extend the analysis of three-point normal loading to $\beta < 90^\circ$ which means that the support reactions are tensile in order to maintain equilibrium, we can find that IP does not occur in the disk for $\beta < 90^\circ$. From Fig. 13, IP starts forming in the disk just after $\beta = 90^\circ$, moves rapidly towards center with decreasing rate with β as β increases to 120° . When β varies from 90° to 180° , IP moves from center to lowest periphery almost with steady rate.

Now, the three-point loading of disk is analyzed with $\beta = 135^\circ$ and the two bottom reactions are made arbitrary

to take friction into account, keeping the symmetry about y -axis as shown in Fig. 14(a). μ is coefficient of friction at the supports.

For the disk to be in static equilibrium in this loading configuration, the top load P and each bottom load Q must satisfy the following condition (Fig. 14(b)).

$$\begin{aligned}
 &2Q \cos(180^\circ - \beta - \arctan \mu) = P \\
 \text{since } \beta &= 135^\circ, \quad 2Q \cos(45^\circ - \arctan \mu) = P \\
 \Rightarrow &2Q \frac{1}{\sqrt{2}} \left(\frac{1}{\sqrt{1 + \mu^2}} + \frac{\mu}{\sqrt{1 + \mu^2}} \right) = P \\
 \therefore &Q = \frac{P}{\sqrt{2}} \frac{\sqrt{1 + \mu^2}}{1 + \mu} \tag{17}
 \end{aligned}$$

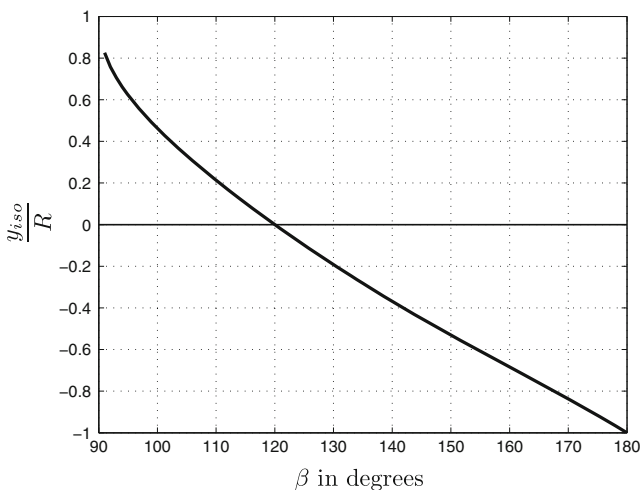


Fig. 13 Position of IP on y -axis of circular disk under three-point normal loading for various β

Solution for the disk under oblique reactions at supports is solved, again using superposition of Flamant problems and hydrostatic term. Solution for pure tangential loading on the disk boundary can be derived using just the Flamant solution (equation (9)) with $\gamma = 90^\circ$. Difference between the pure normal loading and pure tangential loading, using Flamant solutions approach, is as follows. Self-equilibrating pure normal loading induces uniform radial stress at periphery whereas pure tangential loading does not induce any amount of traction at periphery provided net moment due to the loads is zero. To prove the last statement, one may consider the disk under static equilibrium with four equal tangential loads with alternating directions of clock-wise and counter clock-wise equally spaced on the boundary. Therefore, the residual traction on the disk boundary after superposing three Flamant problems of one normal load



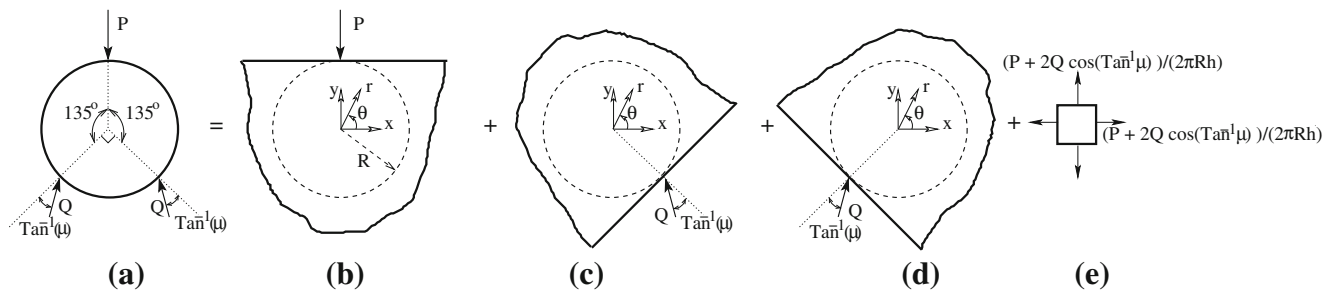


Fig. 14 (a) Circular disk under three-point loading with the two arbitrary support reactions simulating the experimental loading (b–e) Solution algorithm: Superposing Flamant problems and hydrostatic solution

and two oblique reactions, would be again a constant radial stress of magnitude $\sum P^{(N)} / (2\pi Rh)$ where:

$$\begin{aligned} \sum P^{(N)} &= P + Q \cos(\arctan \mu) + Q \cos(\arctan \mu) \\ &= P + 2Q / \sqrt{1 + \mu^2} \\ &= P \left(\frac{1 + \mu + \sqrt{2}}{1 + \mu} \right). \end{aligned} \tag{18}$$

The stresses in the disk under oblique reactions is given below only schematically as it is again unwieldy to present complete expressions.

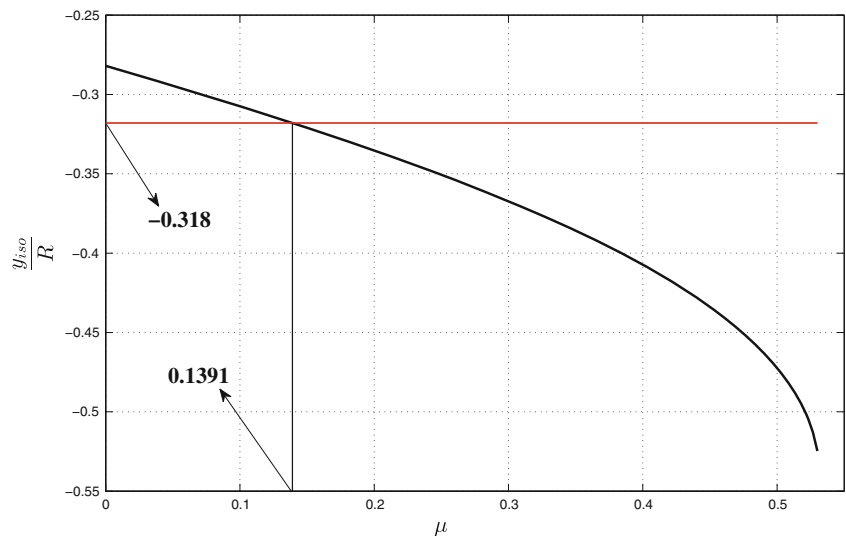
$$\begin{aligned} [\tilde{\sigma}^{3pt}] &= [\tilde{\sigma}^{(d)}]_{\alpha = 0^\circ, \gamma = 0^\circ} + [\tilde{\sigma}^{(d)}]_{\alpha = 135^\circ, \gamma = -\arctan \mu, P = Q} \\ &\quad + [\tilde{\sigma}^{(d)}]_{\alpha = -135^\circ, \gamma = \arctan \mu, P = Q} + [\tilde{\sigma}^{Hy}] \end{aligned} \tag{19}$$

The IP positions, obtained by solving equation (16), are plotted in Fig. 15 with varying friction coefficient when the

disk is subjected to three loads. From the plot, it can be inferred that y_{iso} varies in a non-linear fashion with μ and the curve of absolute value $|y_{iso}|$ as a function of μ , has consistently increasing slope with a vertical tangent at the end where the IP disappears. Experimentally measured position of IP from Fig. 5 is drawn as an ordinate in Fig. 15 to determine which μ value corresponds closest to the experiment. And it is determined from Fig. 15 that $\mu^{exp} = 0.139$. Thus coefficient of static friction, that is aroused for the three-point loading, is 0.139.

Isochromatics pattern for this particular case of $\mu = 0.139$ is shown in Fig. 16 along with experimental result reproduced from Fig. 5 for easy comparison. It can be observed from the figure that theoretical isochromatics pattern matches well with the experimental one validating our method of calibrating friction using solely IP location. However, the fringe pattern may deviate slightly at close vicinity of the load regions since the loads are modeled as concentrated ones in the analysis. It can also be inferred from Fig. 16(a) that $N = 0$ moves away from the bottom periphery towards the center of the disk for non-zero μ whereas it forms along periphery for pure normal loading case. Since $|y_{iso}|$ increases with μ from Fig. 15, we infer that IP moves

Fig. 15 Position of IP on y-axis of circular disk under 3 point oblique loading for various μ



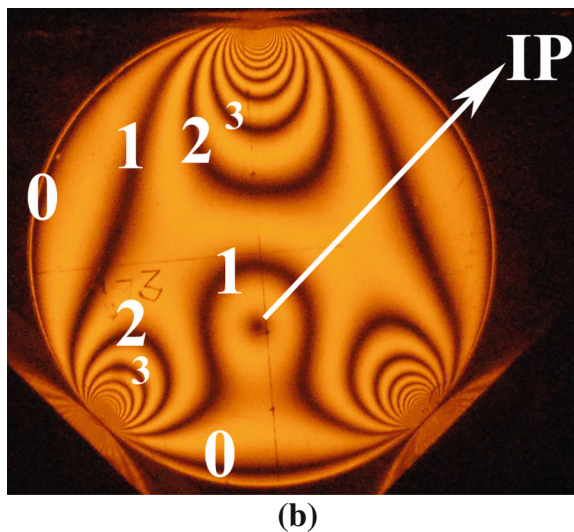
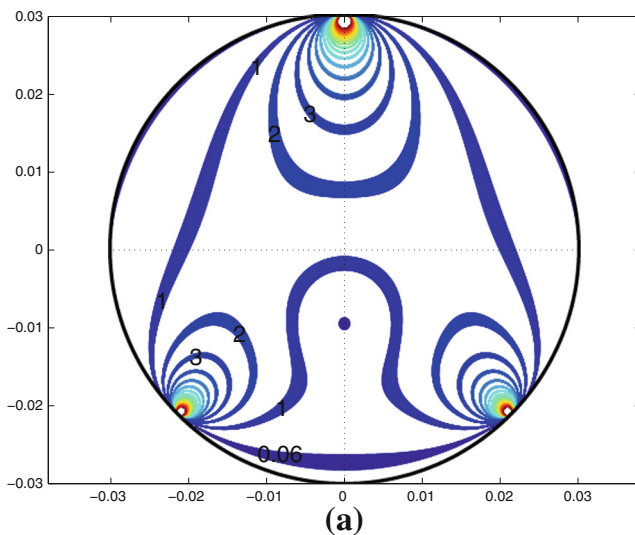


Fig. 16 Isochromatics of circular disk under three-point loading (a) theoretical result with oblique reactions ($\mu = 0.139$) (b) experimental result

away from the center as μ increases. If we extend the 3-point loading analysis further for higher μ , at certain μ , IP and $N = 0$ from bottom merge with each other beyond which neither IP nor $N = 0$ forms inside the disk region.

Four-Point Loading Results

Circular disk under four-point loading symmetric about x and y axes, shown in Fig. 17, is analyzed similar to the three-point loading case. Each of the four loads are kept inclined to keep the generality. Method of solving to arrive to exact solution of the problem with point loads are very similar to the three-point loading case.

It is solved first with pure normal loading which means $\mu = 0$ and $Q = P/(2 \cos \beta)$ for various β taking

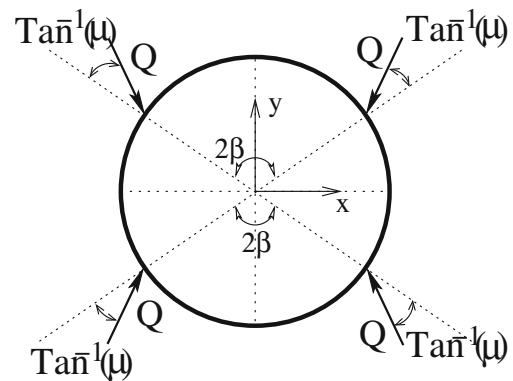


Fig. 17 Circular disk under four normal and four tangential point loads acting in four-fold symmetric manner on its periphery

$P = 869$ N (same as the experimental load in Fig. 7 of section “**Isochromatic Results**”), $R = 0.03$ m, $h = 0.006$ m and $f_\sigma = f_\sigma^B$ from last paragraph of section “**Calibration of the Specimens for f_σ** ”. Isochromatics patterns for two cases $2\beta = 90^\circ$ and 99° are plotted in Fig. 18.

We can observe from the figure that there is only one IP at the center in case of $2\beta = 90^\circ$. Isochromatic pattern has 8-fold symmetry as the loading dictates. There are two IPs forming on x -axis symmetric about y -axis in case of $2\beta = 99^\circ$. The distance of IP from center along positive x -axis, x_{iso} , when 2β varies from 90° to 180° , is plotted in Fig. 19. The characteristic of the curve in Fig. 19 is similar to that of three-point normal loading case in Fig. 13. The x_{iso} curve varies non-linearly initially and almost linearly at higher β values. From the figure, we can conclude that the symmetric pair of IPs move towards each other along x -axis as 2β varies from 180° to 90° . At $2\beta = 90^\circ$ the two IPs coalesce with each other forming one IP exactly at the center of the disk. When we extend the analysis for 2β varying from 90° to 0° , the symmetric pair of IPs shift their positions to y -axis and they move away from each other along y -axis. The shift of IPs between the axes is expected as the loading when $2\beta : 180^\circ - 90^\circ$, is mirror image of that when $2\beta : 90^\circ - 0^\circ$, with the mirror being $2\beta = 90^\circ$ case.

Let us consider *non-zero* friction coefficient (μ) at the four load points on the disk, as shown in Fig. 17. To capture only the effect of μ , we need to fix 2β . Using the measured inter-point distances from equation (5) of Fig. 8, approximately 2β is fixed to be 99° . And symmetric formulation with $\mu \neq 0$ is used to predict the isochromatics pattern in Fig. 7 using IPs information. Circular disk under 4 oblique loads acting symmetrically on its boundary is solved for various values of $\mu = 0, 0.01, 0.02, \dots, 1$ by taking $Q = P/2 / \cos(99^\circ/2 - \arctan \mu)$, $P = 869$ N, $R = 0.03$ m, $h = 0.006$ m and $f_\sigma = f_\sigma^B$. In each case, position of IPs, $\pm x_{iso}$ is obtained by solving the problem numerically

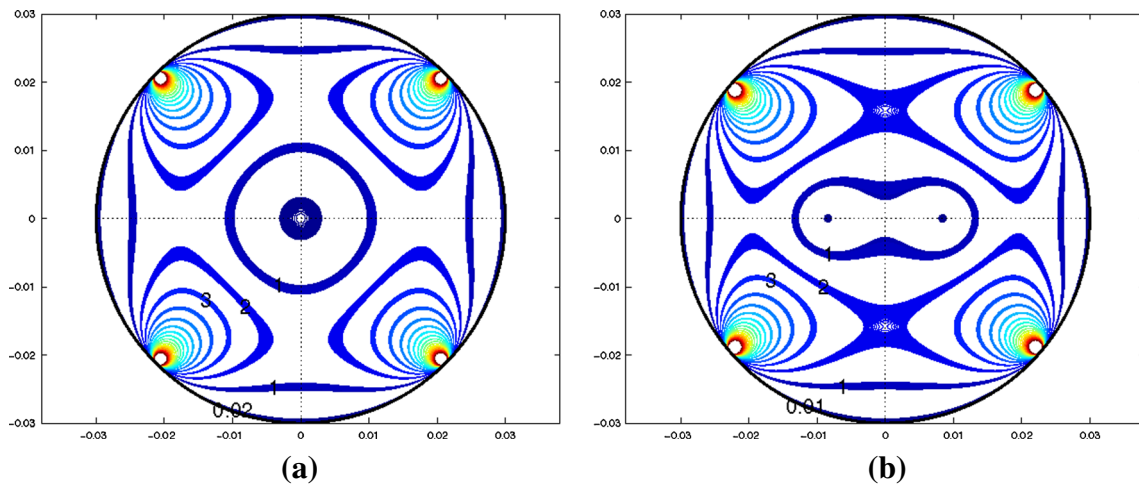


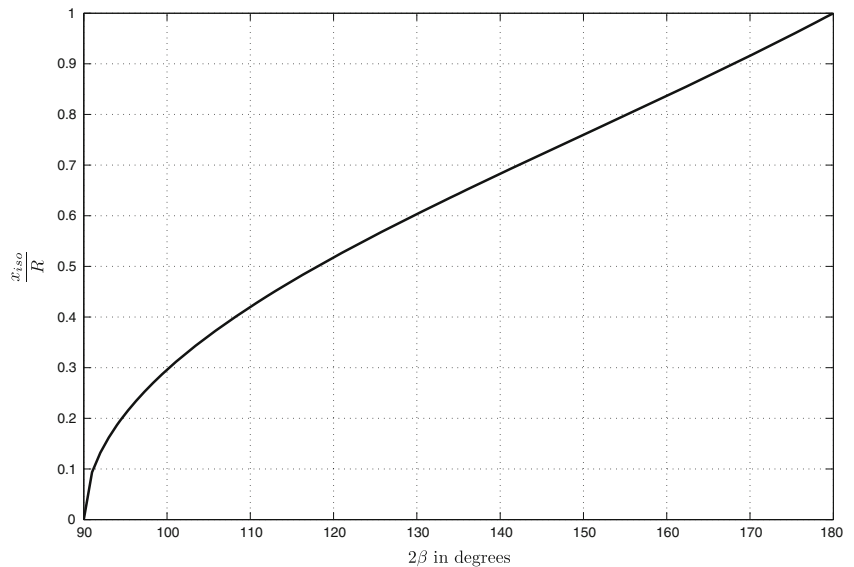
Fig. 18 Isochromatics of circular disk under 4 point normal loading for (a) $2\beta = 90^\circ$ (b) $2\beta = 99^\circ$

using MATHEMATICA and plotted in Fig. 20. Experimentally obtained value of $x_{iso}/R = 4.45/16.4 = 0.2713$ from equation (5) is provided as an ordinate in the plot which meets the curve at $\mu^{exp} = 0.155$ which is the required active coefficient of friction between disk and fixture surfaces.

Isochromatics for the particular case of $2\beta = 99^\circ$ and $\mu = 0.155$ is plotted in Fig. 21(a). Corresponding experimental result is reproduced as Fig. 21(b) from section “Isochromatic Results” for ease of comparison.

From Fig. 21(b), ZOF is moved inwards from periphery at top and bottom portions which phenomenon is well predicted by theory (Fig. 21(a)). In an overall sense, the theoretical result matches closely with the experimental one again validating our concept of theoretical interpretation using IPs.

Fig. 19 Distance of IP from center of the disk along positive x-axis for different β



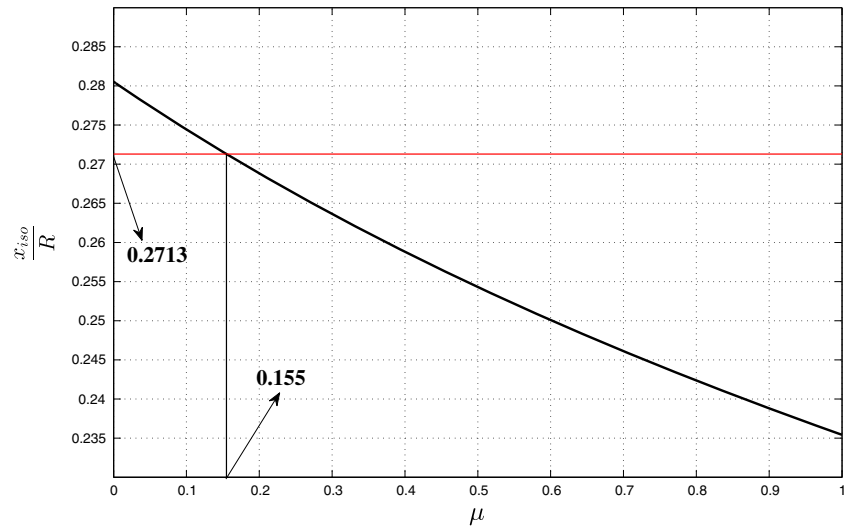
Analysis of Isochromatics under Hertzian Loads

Figure 22 shows a magnified view of isochromatics pattern near load region of circular disk under diametral compression which highlights the intricately artistic complexity of an experimental fringe pattern culled from the archives of the Photoelastic laboratory. This pattern clearly portrays a bifurcation about the symmetric loading axis. The two distinctly clear isolated points occurring inside isochromatic loops subtly suggest some frictional shear in addition to the normal pressure. Conventional Hertzian analysis without friction predicts a single isolated point directly beneath the applied load along the axis of symmetry.

In this section, a theoretical interpretation by including two symmetric frictional shear Hertzians in addition to the normal stress Hertzian, is attempted to explain the splitting



Fig. 20 Distance of IP from center of the disk along positive x -axis for different μ when $2\beta = 99^\circ$



of fringes at close vicinity of applied load in circular disk under diametral compression and other similar situations. For demonstration, circular disk under diametral compression is considered with each of the two loads as having Hertzian normal and a bi-Hertzian tangential distribution, as shown in Fig. 23. Due to symmetry of the problem about x -axis, only upper half is shown.

Hertzian normal and tangential loads are expressed as follows in terms of α which is an angular coordinate defined along periphery from y -axis towards x -axis as shown in Fig. 23 and is therefore equal to $(\pi/2 - \theta)$.

$$p(\alpha) = \frac{-2P}{\pi R \delta} \sqrt{1 - \frac{\alpha^2}{\delta^2}} \quad \text{when } -\delta \leq \alpha \leq \delta \quad (20)$$

$$f(\alpha) = \begin{cases} \frac{2F}{\pi R \delta/2} \sqrt{1 - \frac{(\delta/2 - \alpha)^2}{(\delta/2)^2}} & \text{when } 0 \leq \alpha \leq \delta \\ \frac{-2F}{\pi R \delta/2} \sqrt{1 - \frac{(\delta/2 + \alpha)^2}{(\delta/2)^2}} & \text{when } -\delta \leq \alpha \leq 0 \end{cases} \quad (21)$$

Observe that the multipliers of the Hertzian functions in equations (20) and (21) give the maximum magnitude of the applied tractions and are so calculated that, by integrating the functions along the loaded arc, we can obtain total loads P and F as follows.

$$\int_{\alpha=-\delta}^{\delta} p(\alpha) R d\alpha = -P$$

$$\int_{\alpha=0}^{\delta} f(\alpha) R d\alpha = F = - \int_{\alpha=-\delta}^0 f(\alpha) R d\alpha \quad (22)$$

Stresses in the disk under the Hertzian loading is obtained using again Flamant solution expressed in a general coordinate system in section “Method”. Substituting $p(\alpha) R d\alpha$ for P and taking $\gamma = 0^\circ$ in equation (9) makes it differential stress tensor required to be integrated for complete normal loading. Similarly substituting $-f(\alpha) R d\alpha$ for P and taking

$\gamma = 90^\circ$ in equation (9) makes it differential stress tensor for complete tangential loading. Integrating the differential stress components along the loaded arc, from $-\delta$ to δ (for top load) and from $(\pi - \delta)$ to $(\pi + \delta)$ (for bottom load) as follows,

$$\begin{aligned} [\tilde{\sigma}^{Hertz(a)}] &= \int_{\alpha=-\delta}^{\delta} [\tilde{\sigma}^{(d)}]_{P=p(\alpha) R d\alpha} \gamma=0^\circ \\ &+ \int_{\alpha=\pi-\delta}^{\pi+\delta} [\tilde{\sigma}^{(d)}]_{P=p(\alpha) R d\alpha} \gamma=0^\circ \\ &+ \int_{\alpha=-\delta}^{\delta} [\tilde{\sigma}^{(d)}]_{P=-f(\alpha) R d\alpha} \gamma=90^\circ \\ &+ \int_{\alpha=\pi-\delta}^{\pi+\delta} [\tilde{\sigma}^{(d)}]_{P=-f(\alpha) R d\alpha} \gamma=90^\circ \end{aligned} \quad (23)$$

would leave a uniform radial stress of $-2P/(2\pi Rh)$ on the disk periphery. This indicates that the integration is nothing but superposition of many Flamant problems as expected. The integrals are evaluated individual component-wise numerically using MATLAB. The residual radial stress on the boundary is annihilated by superposing a hydrostatic tension to give the required solution for the circular disk under diametral Hertzian compression and bi-Hertzian shear, as follows.

$$[\tilde{\sigma}^{Hertz}] = [\tilde{\sigma}^{Hertz(a)}] + \frac{2P}{2\pi Rh} \begin{bmatrix} 1 & 0 \\ 0 & 1 \end{bmatrix} \quad (24)$$

Isochromatics are plotted taking $P = 790 \text{ N}$, $f_\sigma = 13458 \text{ N/m/fringe}$, $\delta = 3^\circ$ and $F = 0.135P$ as shown in Fig. 24(a). Only 13 fringe orders $N = 0-12$ are shown in Fig. 24(a). In an overall sense, the fringe pattern is same as



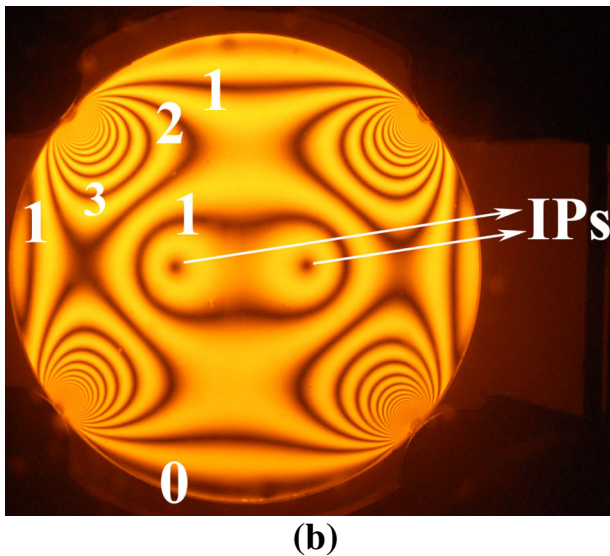
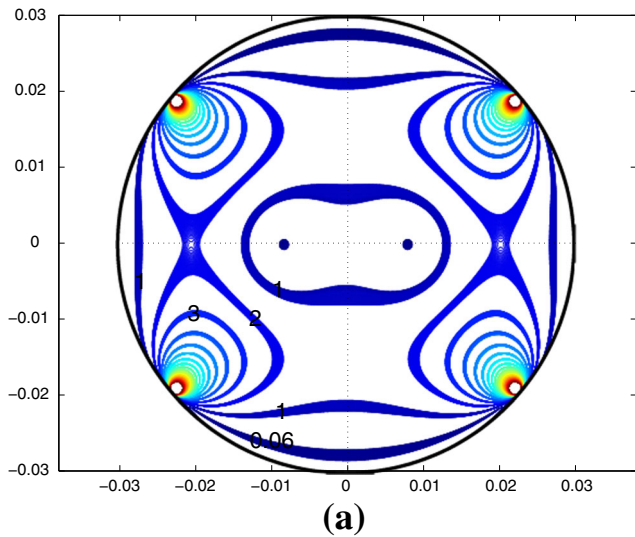


Fig. 21 Isochromatics of circular disk under (a) 4 oblique loads with $\mu = 0.155$ when $2\beta = 99^\circ$, theoretical result (b) four-point loading, experimental result

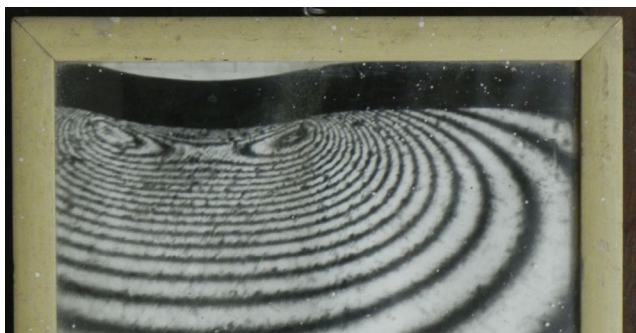


Fig. 22 Magnified view of Isochromatic fringe pattern near upper load region of circular disk under diametral compression

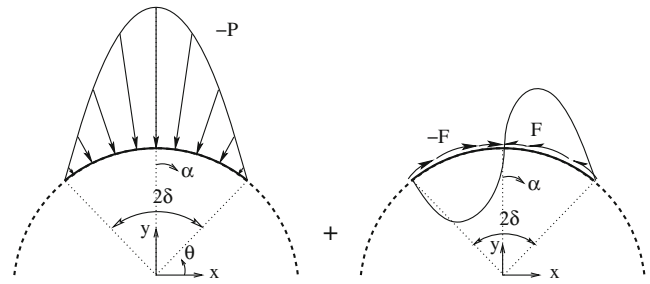


Fig. 23 Contact load modeled as Hertzian normal load coupled with bi-Hertzian tangential load and viewed as superposition of the two

that of point load case ($\delta = 0^\circ$) where shear tractions cancel themselves as they are equal in magnitude and opposite in direction acting at the same point of loading. Isochromatics pattern is magnified at the top load-region and shown in Fig. 24(b) where fringe orders from $N = 8$ to $N = 23$ are plotted.

Figure 24(b) presents a close-up of isochromatics just underneath the Hertzian loading with friction. From Fig. 24(b), $N = 14$ splits into two loops enveloped partially by $N = 13$ and partially by itself. This phenomenon cannot be found in case of pure normal loading whether the load is distributed or concentrated. Therefore, splitting of fringes observed in Fig. 22 can be attributed partially to shear caused by incipient sliding traction along the contact though the loading is macroscopically normal. The zoomed-in isochromatics of the disk near the loading is produced for various tangential load values, $F/P = 0.000, 0.001, \dots, 0.300$ and animated into a video *CirHertzZoom4.mpg* which is provided as Online Resource 1.

From the animation, set of fringes very close to the loaded curve and those intersect the boundary, forms directly beneath the loaded curve of the boundary. The fringe order N decreases first from the periphery, reaches a minimum value and increases to a maximum value and then steadily decrease until center of the disk along y -axis. The maximum point on the y -axis is where the splitting occurs. At the point of minimum, a fringe-loop forms which is in between the top portion of boundary and the split-fringe. The point of minimum value moves inwards from boundary as F/P increases from 0 to nearly 0.145 from where it ceases to form single loop. Complete splitting of $N = 14$ can be observed at $F/P \approx 0.125$. Nucleation of $N = 15$ inside $N = 14$ occurs when $F/P \approx 0.155$. Observe that $N = 14$ splits from its parent single loop whereas $N = 15$ nucleates by itself as two loops. At $F/P \approx 0.175$, $N = 15$ starts merging with its other part and ceases to be two loops. Within a short span of $F/P \approx 0.205 - 0.215$, pair of fringe-loops of $N = 16$ form and coalesce with its other part. Further split-fringe can be hardly seen for $N > 16$. In addition to the above phenomena which occur more or less near

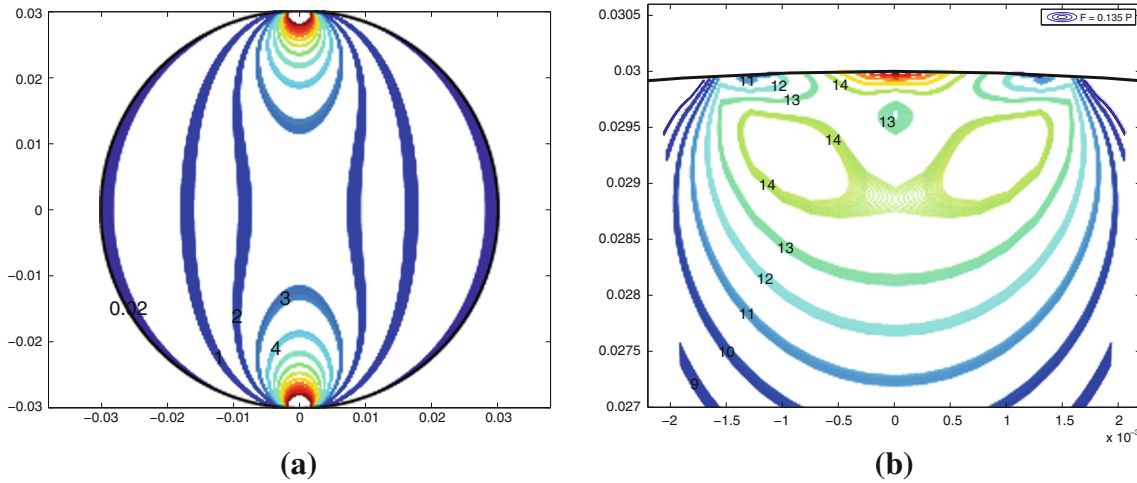


Fig. 24 Isochromatics of circular disk under diametral Hertzian compression coupled with bi-Hertzian shear, $F = 0.17P$ (b) Magnified view of isochromatics near load region

the y -axis, almost for all F/P considered, evolution and coalescence of a pair of fringe-loops can be seen close to the boundary and farther from y -axis.

Elasticity Solution of Semicircular Ring

Semicircular ring under a *symmetric* loading on its curved boundaries with traction-free straight edges shown in Fig. 25 is solved for stresses in this section [27]. General formulation and method of solving are extended here to solve the problem on hand. Boundary conditions of the problem are as follows.

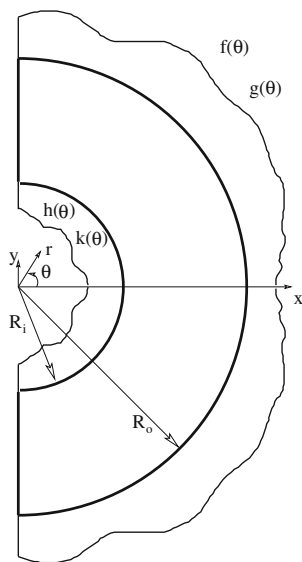


Fig. 25 Semicircular ring with boundary conditions

On the straight edges and on the line of symmetry

$$\left. \begin{aligned} \sigma_{\theta\theta}(r, \theta = \pi/2) = 0 = \tau_{r\theta}(r, \theta = \pi/2) \\ \tau_{r\theta}(r, \theta = 0) = 0 = u_{\theta}(r, \theta = 0) \end{aligned} \right\} \text{when } R_i \leq r \leq R_o \quad (25)$$

On the circular boundaries

$$\left. \begin{aligned} \sigma_{rr}(r = R_o, \theta) = f(\theta) \\ \tau_{r\theta}(r = R_o, \theta) = g(\theta) \\ \sigma_{rr}(r = R_i, \theta) = h(\theta) \\ \tau_{r\theta}(r = R_i, \theta) = k(\theta) \end{aligned} \right\} \text{when } 0 \leq \theta \leq \pi/2 \quad (26)$$

Method

Airy stress function for the problem is chosen from the generalized solution given in the text by Little [13] as:

$$\begin{aligned} \phi = c_5' \left(\frac{r}{R_i} \right) \theta \sin \theta \\ + \sum_{n=-\infty, \infty}^{-\infty, \infty} \left[a_n \left(\frac{r}{R_i} \right)^n + b_n \left(\frac{r}{R_i} \right)^{n+2} \right] \cos n\theta \end{aligned} \quad (27)$$

The only non-series term in the chosen stress function which is Flamant term, $(r\theta \sin \theta)$ is considered to take care of the fact that material is absent at the origin (center of the ring). This term gives rise to singular stresses at origin. The other terms of the generalized Airy stress function which also give singular stresses at origin, are not considered since their contribution to the solution can be easily proved to be nil using the straight boundary conditions presented by equations (25). Using the same straight boundary



conditions, the following relations between the coefficients can be derived.

$$\begin{aligned}
 b_n &= a_{n+2} \quad \text{where } n \text{ is even} \\
 nb_n &= (n + 2)a_{n+2} \quad \text{where } n \text{ is odd}
 \end{aligned}
 \tag{28}$$

Stress components can be derived from the stress function (27) using equation (6). Using the relations (28) in the expressions for stress components and rearranging them gives:

$$\begin{aligned}
 \sigma_{rr}(r, \theta) &= - \sum_{n=\dots, -2, 0, 2, \dots}^{-\infty, \infty} [n \cos n\theta + (n - 4) \cos (n - 2)\theta] (n - 1) \frac{a_n}{R_i^2} \left(\frac{r}{R_i}\right)^{n-2} \\
 &\quad - \sum_{n=\dots, -1, 1, \dots}^{-\infty, \infty} \left[\cos n\theta + \frac{n - 4}{n - 2} \cos (n - 2)\theta \right] n(n - 1) \frac{a_n}{R_i^2} \left(\frac{r}{R_i}\right)^{n-2} + \frac{c_5'}{R_i^2} \frac{2 \cos \theta}{r/R_i}
 \end{aligned}
 \tag{29}$$

$$\begin{aligned}
 \sigma_{\theta\theta}(r, \theta) &= \sum_{n=\dots, -2, 0, 2, \dots}^{-\infty, \infty} [\cos n\theta + \cos (n - 2)\theta] n(n - 1) \frac{a_n}{R_i^2} \left(\frac{r}{R_i}\right)^{n-2} \\
 &\quad + \sum_{n=\dots, -1, 1, \dots}^{-\infty, \infty} \left[\cos n\theta + \left(\frac{n}{n - 2}\right) \cos (n - 2)\theta \right] n(n - 1) \frac{a_n}{R_i^2} \left(\frac{r}{R_i}\right)^{n-2}
 \end{aligned}
 \tag{30}$$

$$\begin{aligned}
 \tau_{r\theta}(r, \theta) &= \sum_{n=\dots, -2, 0, 2, \dots}^{-\infty, \infty} [n \sin n\theta + (n - 2) \sin (n - 2)\theta] (n - 1) \frac{a_n}{R_i^2} \left(\frac{r}{R_i}\right)^{n-2} \\
 &\quad + \sum_{n=\dots, -1, 1, \dots}^{-\infty, \infty} [\sin n\theta + \sin (n - 2)\theta] n(n - 1) \frac{a_n}{R_i^2} \left(\frac{r}{R_i}\right)^{n-2}
 \end{aligned}
 \tag{31}$$

Now the set of unknown coefficients, a_n for $n = \dots, -2, -1, 0, 2, 3, \dots$, is to be determined using the four conditions on curved boundaries given by the set of equations (26). This is done using collocation method. A finite number of points b are chosen on each of the curved boundaries (only upper half is modeled due to symmetry) and the corresponding boundary conditions are satisfied at each of these points simultaneously, with a truncated series of stress function, by formulating the whole problem at this stage as a set of linear equations. Solving the linear equations gives the finite number of unknowns a_n , coefficients of truncated stress function. Thus the problem is solved.

The results are sensitive to the number of collocation points b chosen, especially near the curved boundaries. By increasing b we can improve accuracy of result.

Results of Analysis

To arrive to the result in Fig. 9(a), the loading on the semi-circular ring is modeled as three-point Hertzian loading as shown in Fig. 26(a). The Hertzian load acting at inner boundary is assumed to be purely horizontal (y -component of the traction is zero at any point) whereas the symmetric pair of Hertzian loads acting on outer boundary are kept arbitrary for analysis to identify friction. Corresponding idealized loading model shown in Fig. 26(b) with all point loads in place of Hertzian loads yields the following

relationship among the total load magnitudes using equilibrium equations.

$$Q \cos \beta + F \sin \beta = \frac{P}{2} \implies Q = \frac{P}{2 \cos \beta} - F \tan \beta
 \tag{32}$$

Loading functions defined in equation (26) for upper half of the curved boundaries, take the following form for

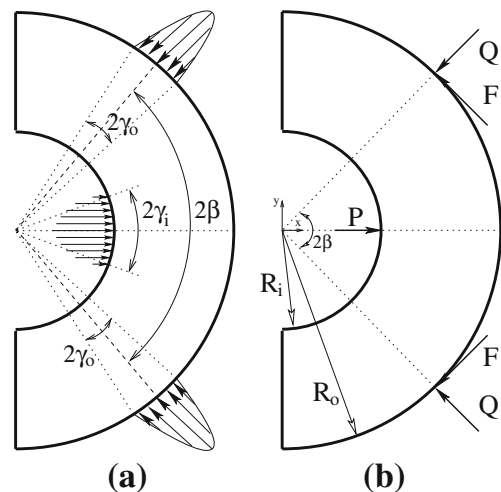


Fig. 26 Semicircular ring under three-point loading (a) Hertzian loads (b) 3 normal and 2 tangential point loads



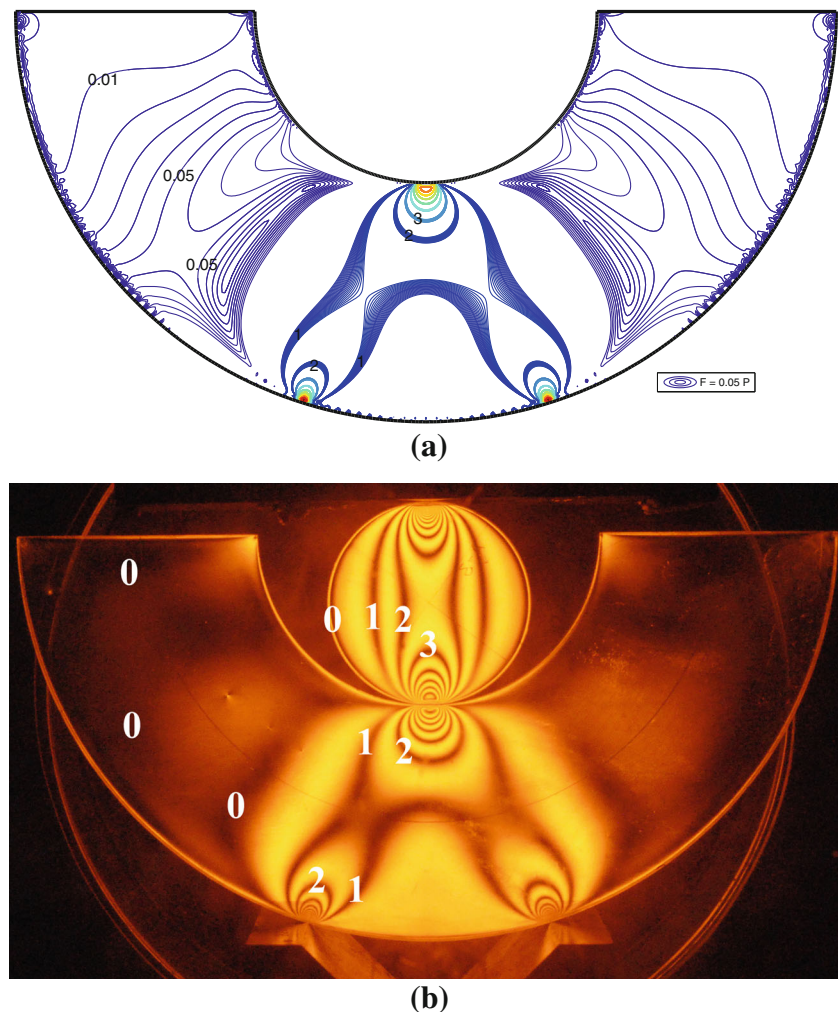
the problem of semicircular ring under three-point Hertzian loading.

$$\begin{aligned}
 f(\theta) &= \frac{-2Q}{\pi R_o \gamma_o h} \sqrt{1 - \frac{(\theta - \beta)^2}{\gamma_o^2}} \quad \text{when } (\beta - \gamma_o) \leq \theta \leq (\beta + \gamma_o) \\
 g(\theta) &= \frac{2F}{\pi R_o \gamma_o h} \sqrt{1 - \frac{(\theta - \beta)^2}{\gamma_o^2}} \quad \text{when } (\beta - \gamma_o) \leq \theta \leq (\beta + \gamma_o) \\
 h(\theta) &= \frac{-2P}{\pi R_i \gamma_i h} \sqrt{1 - \frac{\theta^2}{\gamma_i^2}} \cos \theta \quad \text{when } 0 \leq \theta \leq \gamma_i \\
 k(\theta) &= \frac{-2P}{\pi R_i \gamma_i h} \sqrt{1 - \frac{\theta^2}{\gamma_i^2}} \sin \theta \quad \text{when } 0 \leq \theta \leq \gamma_i
 \end{aligned} \tag{33}$$

where Q is given by equation (32), and γ_i and γ_o are semi-Hertzian load angles of inner and outer loads respectively as shown in Fig. 26(a). -ve sign for P and Q is due to compressive nature of the loads and +ve sign for F is due to that it is acting in the direction of increasing θ on the outer face whose outer normal is directed towards increasing r .

Total $b = 121$ are chosen on each of the curved boundaries including end points and the problem is solved for various values of $F/P = 0.002, 0.004, \dots, 0.2$ taking $R_o = 0.1205$ m, $R_i = 0.05025$ m, $h = 0.006$ m, $\beta = 17.3829^\circ$, $2\gamma_o = 1^\circ$, $2\gamma_i = 6^\circ$, $P = 790$ N and $f_\sigma^A = 13458$ N/m/fringe. The problem is modeled and solved in vertical configuration of the ring so that the resulting stress function (equation (27)) becomes simple with only even functions of θ . But the isochromatic results are plotted with horizontal configuration of the ring by rotating the stresses appropriately so that we can compare with the experimental result easily. Hertzian angle for inner load is chosen so much since the concave side of the ring is contacting with convex side of the calibration disk and that for outer load is chosen so small since the ring is contacting an edge. The Hertzian angles of outer and inner loads does not affect stress distribution in the ring in an overall sense until certain magnitudes according to St. Venant principle. Maximum fringe order that forms near the contact decreases with the load distribution angle.

Fig. 27 Isochromatics of semicircular ring under three-point loading (a) Hertzian loads with $F/P = 0.05$, theoretical result (b) experimental result



Isochromatics pattern for the case of $F/P = 0.05$ is shown in Fig. 27(a). Experimental isochromatics of semicircular ring under three-point loading from section “[Isochromatic Results](#)” is reproduced as Fig. 27(b) for comparison.

In Fig. 27(a), a small noise at the curved boundaries arises due to truncation of series of stress function and collocation at finite number of points on the curved boundaries. Otherwise, the theoretical result captures almost all the details of experimentally observed isochromatics pattern. $N = 1$ forms a closed loop resembling the English alphabet ‘A’ which is in agreement with experimental result. Since there are no IPs formed in this case, we can only arrive to approximate F/P by qualitative observations. However, using recent advances in digital photoelasticity (see, for example, [28]), *non-zero* fringe orders can be located with high accuracy. The results of digital analysis in conjunction with analytical solution derived here can be used for theoretical interpretation.

Discussion

Location of ZOF and IPs, is independent of f_σ , h and magnitude of a reference load ($= P$ in this paper) making the method presented here an elegant one. Since all these quantities are directly proportional to fringe order N , since N at IP is *zero* they do not play any role. But IP location does depend on loading configuration allowing us to study its migration with loading configuration. This property is not exhibited by *non-zero* fringe orders. All of them vary linearly with the quantities mentioned. All these facts are valid only in 2D analysis. In addition, state of stress is independent of thickness (h) for given load per unit thickness in *plane* problems. For given total load (in N), all the three stress components vary as $1/h$. However, when a crack exists in the disk, fracture toughness does depend on thickness, as for example studied by Aliha [29].

In four-point loading of circular disk, when tangential components of loads are also considered along with normal components, ZOF moves inwards from top and bottom as tangential component increases. And it is expected to move outwards (outside the region of disk) from left and right to form a complete ellipse. With the increase of tangential component, eccentricity (slenderness) of the ellipse increases. Shear traction associated with normal traction at loading contact is found to cause splitting of fringes at close vicinity of loaded boundary.

To transform state of stress in a semi-infinite plate due to a point load, to a different coordinate system, we changed the coordinates in Airy function which is the simplest procedure. Alternatively, one can follow the longer procedure of transformation of stress tensor [30] to arrive to stress

components in a different coordinate system. Circular disk under pure normal loading on its periphery can be derived also with the help of Michell’s solution for circular disk under two collinear point loads one at the center the other at the periphery [16]. By superposing different variants of Michell’s solution, we can solve any normal loading on boundary of the disk. Singularity of stresses at the center due to point load there, is completely removed as the point loads from the different variants self cancel themselves giving rise to *zero* load at the center. For this, superposed loads on the periphery must be self-equilibrating which is always ensured. This method does not need hydrostatic solution for annihilation of residual traction at the boundary since all the sub-problems being superposed involve finite geometries, have self-equilibrating loading and traction-free boundaries.

Analysis of circular disk under four normal loads in section “[Four-Point Loading Results](#)” with $2\beta = 90^\circ$ (8-fold symmetry) is shown to have one IP at the center using the animation (Online Resource 1). Also it has been shown that same problem with a given $2\beta (\neq 90^\circ)$ gives rise to two IPs with their separation varying with tangential loading. In case of $2\beta = 90^\circ$ there is only one IP forming at the center for any amount of tangential component. Tangential loads at the four contact points do not affect the position of IP in this special case of $2\beta = 90^\circ$. Therefore, $2\beta^{exp} = 99^\circ$ in case of four-point loading explained in section “[Isochromatic Results](#)” enables us studying IP location.

The loading configurations of circular disk analyzed in this paper, can be extended to asymmetric loading type. For example, three-point loading of the disk can be modified to promote asymmetry by moving the top load point to some other point on the periphery as shown in Fig. 28. This configuration can be realized by using the same V-block for the bottom supports and keeping the top loading bar inclined. The V-block must be fixed to the loading frame to avoid sliding of the block on the frame. In the asymmetric configuration, the top load P , must also be inclined to radial direction in order to balance the moment due to unequal support reactions. This implies a *non-zero* friction between disk surface and the loading bar. Thus the asymmetric loading introduces another degree of freedom of friction coefficient

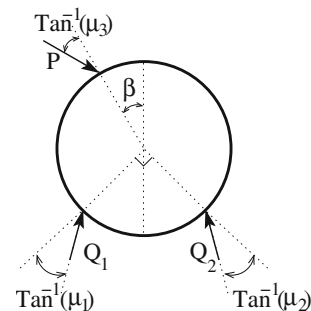


Fig. 28 Circular disk under asymmetric 3-point loading

into the problem. To find the magnitude of load (P) that is transferred between the loading bar and the disk using rigid-body analysis of the loading bar, coefficient of friction at the bar-disk contact must be given. Then, the equilibrium of disk under three inclined forces with one force (P) known along with its inclination, gives three equations leaving one parameter to vary. This is our current topic of research.

Regarding the feasibility of the three-point and four-point loadings of the disk: one has to exercise enough care while loading to avoid asymmetries. Also, V-block or four-point fixture needs to be fabricated with sufficient accuracy on surface roughness. Disk under diametral compression may be far simpler. But, there are no isotropic points formed in the disk and characterizing friction in this configuration is seldom possible.

Conclusion

Isochromatics of circular disk under three-point loading showed a deviation from exact radial distribution of fringes at the supports. Using analytical solution for circular disk loaded at its periphery in conjunction with the concept of IP in experimental fringe patterns, the deviation of fringe pattern at the supports is explained. A *non-zero* frictional shear at the supports is found to cause the deviation. Analysis of the disk under four-point loading with oblique loads emphasizes the presence of shear at the load points. Analysis of semicircular ring under three-point loading with sharp supports also reveals the effect of friction qualitatively. Splitting of fringes at close vicinity of distributed loads is explained by the association of normal load with a distributed shear load. It can be concluded that active coefficient of friction can be determined by isochromatics pattern provided by photoelastic technique.

Acknowledgments Authors would like to acknowledge Mr. G. Babu, the lab-technician for his help during experiments and Dr. M. Ramesh for his help while obtaining theoretical solutions.

References

- Dally JW, Chen YM (1991) A photoelastic study of friction at multipoint contacts. *Exp Mech* 31:144–149
- Uemura Y, Takai M, Takemura K (1950) Measurement of the coefficient of friction by the photo-elastic method (I). Technical report, Institute for Chemical Research, Kyoto University. http://repository.kulib.kyoto-u.ac.jp/dspace/bitstream/2433/74201/1/chc023_052.pdf
- Uemura Y, Takai M (1952) Measurement of the coefficient of friction by the photo-elastic method (II). Technical report, Institute for Chemical Research, Kyoto University. http://repository.kulib.kyoto-u.ac.jp/dspace/bitstream/2433/74373/1/chc027_050.pdf
- Comninou M (1976) Stress singularity at a sharp edge in contact problems with friction. *J App Math Phys* 27:493–499
- Burguete RL, Patterson EA (1997) A photoelastic study of contact between a cylinder and a half-space. *Exp Mech* 37:314–323
- Fedorchenko IM, Kovynev RA, Makovetskii VA, Sitnikov LL (1968) A photoelastic technique for examining contact stresses in powder compaction. *Poroshkovaya Metallurgiya* 71:850–854. translated version
- Barbat SDK, Rao RS (1990) Photoelastic investigation of metal-forming processes using new sapphire dies. *Exp Tech* 6:40–43
- Foust B, Lesniak J, Rowlands R (2011) Determining individual stresses throughout a pinned Aluminum joint by reflective photoelasticity. *Exp Mech* 51:1441–1452
- Cheng-yao G, Jia-fu Q, Nan-sheng Q, Guo-chun Z, Hou-he Z, Qiao Y, Xiang-dong B, Chao W (2013) The relationship between the friction coefficient and the asperities original inclination angle. *Res J Appl Sci Eng Technol* 6(11):1906–1910. <http://maxwellsci.com/print/rjaset/v6-1906-1910.pdf>. Accessed 9 March 2014
- Frocht MM (1941) Photoelasticity, vol 1. Wiley, New York
- Ramesh M, Kailas SV, Simha KRY (2008) Near surface stress analysis strategies for axisymmetric fretting. *Sadhana* 33:273–297
- Timoshenko SP, Goodier JN (1970) Theory of elasticity, 3rd edn. McGraw-Hill Book Company, Singapore
- Little RW (1973) Elasticity. Prentice-Hall Inc., New Jersey
- Johnson KL (1987) Contact mechanics. Cambridge University Press
- Coker EG, Filon LNG (1957) A treatise on photo-elasticity. Cambridge University Press
- Michell JH (1900) Elementary distribution of plain stress. In: Proceedings of the London mathematical society, vol 32, p 44
- Mindlin RD (1937) Stress systems in a circular disk under radial forces. *J Appl Mech* 1:41–44
- Ma C-C, Hung K-M (2008) Exact full-field analysis of strain and displacement for circular disks subjected to partially distributed compressions. *Int J Mech Sci* 50:275–292
- Surendra KVN, Simha KRY (2013) Synthesis and application of weight function for edge cracked semicircular disk (ECSD). *Engng Fract Mech* 107:61–79. doi:10.1016/j.engfracmech.2013.05.010
- Dini D, Hills DA (2009) Frictional energy dissipation in a rough hertzian contact. *J Tribol Trans ASME* 131:021401–1–021401–8
- Ayatollahi MR, Mirsayar MM, Dehghany M (2011) Experimental determination of stress field parameters in bi-material notches using photoelasticity. *Mater Des* 32:4901–4908
- Mirsayar MM, Samaei A (2013) Photoelastic study of bi-material notches: effect of mismatch parameters. *Eng Solid Mech* 1:21–26
- Mirsayar MM (2013) Calculation of stress intensity factors for an interfacial notch of a bi-material joint using photoelasticity. *Eng Solid Mech* 1. doi:10.5267/j.esm.2013.09.006
- Zakeri M, Ayatollahi MR, Guagliano M (2011) A photoelastic study of t-stress in centrally cracked brazilian disc specimen under mode II loading. *Strain* 47:268–274
- Murthy NS, Reddy PV (1987) A manual for experiments in photoelasticity, vol 1. Department of Mechanical Engg, IISc, Bangalore
- Surendra KVN (2010) Theoretical and experimental analysis of cracked disks. Master's thesis, Mechanical Engineering, IISc, Bangalore
- Surendra KVN, Simha KRY Analysis of semicircular ring under symmetric loading. *Eng Fract Mech*
- Simon BN, Ramesh K (2011) Colour adaptation in three fringe photoelasticity using a single image. *Exp Tech* 35:59–65. doi:10.1111/j.1747-1567.2010.00646.x
- Aliha MRM (2013) Indirect tensile test assessments for rock materials using 3-d disc-type specimens. *Arab J Geosci*. doi:10.1007/s12517-013-1037-8
- Jog CS (2007) Foundations and applications of mechanics. In: Continuum Mechanics, 2nd edn, vol 1. Narosa publishing house

